ApJS 2007, COSMOS Special Issue
Preprint typeset using LaTeX style emulateapj v. 10/09/06

THE XMM-*NEWTON* WIDE-FIELD SURVEY IN THE COSMOS FIELD. IV: X-RAY SPECTRAL PROPERTIES OF ACTIVE GALACTIC NUCLEI.

V. Mainieri[1,2], G. Hasinger[1], N. Cappelluti[1], M. Brusa[1], H. Brunner[1], F. Civano[3], A. Comastri[3], M. Elvis[4], A. Finoguenov[1], F. Fiore[5], R. Gilli[3], I. Lehmann[1], J. Silverman[1], L. Tasca[6], C. Vignali[3], G. Zamorani[3], E. Schinnerer[7], C. Impey[8], J. Trump[8], S. Lilly[9], C. Maier[9], R. E. Griffiths[10], T. Miyaji[10], P. Capak[11], A. Koekemoer[12], N. Scoville[11,13], P. Shopbell[11], Y. Taniguchi[14]

ApJS 2007, COSMOS Special Issue

ABSTRACT

We present a detailed spectral analysis of point-like X-ray sources in the XMM-COSMOS field. Our sample of 135 sources only includes those that have more than 100 net counts in the 0.3-10 keV energy band and have been identified through optical spectroscopy. The majority of the sources are well described by a simple power-law model with either no absorption (76%) or a significant intrinsic, absorbing column (20%). The remaining $\sim 4\%$ of the sources require a more complex modeling by incorporating additional components to the power-law. For sources with more than 180 net counts (bright sample), we allowed both the photon spectral index Γ and the equivalent hydrogen column N_H to be free parameters. For fainter sources, we fix Γ to the average value and allow N_H to vary. The mean spectral index of the 82 sources in the bright sample is $<\Gamma>=2.06\pm0.08$, with an intrinsic dispersion of ~ 0.24. Each of these sources have fractional errors on the value of Γ below 20%. As expected, the distribution of intrinsic absorbing column densities is markedly different between AGN with or without broad optical emission lines. We find within our sample four Type-2 QSOs candidates ($L_X > 10^{44}$ erg s^{-1}, $N_H > 10^{22}$ cm^{-2}), with a spectral energy distribution well reproduced by a composite Seyfert-2 spectrum, that demonstrates the strength of the wide field XMM/COSMOS survey to detect these rare and underrepresented sources. In addition, we have identified a Compton-thick ($N_H > 1.5 \times 10^{24}$ cm^{-2}) AGN at z=0.1248. Its X-ray spectrum is well fitted by a pure reflection model and a significant Fe Kα line at rest-frame energy of 6.4 keV.

Subject headings: Surveys – Galaxies: active — X-rays: galaxies – X–rays: general – X–rays:diffuse background

1. INTRODUCTION

Deep pencil-beam surveys with *ROSAT* (Hasinger et al. 1998), *Chandra* (Brandt et al. 2001; Rosati et al. 2002; Cowie et al. 2002; Alexander et al. 2003) and XMM-*Newton* (Hasinger et al. 2001; Loaring et al. 2005) have proved that the majority of the X-ray background (XRB) is generated by Active Galactic Nuclei (AGN) both in the soft (0.5-2 keV) and hard (2-10 keV) band. At fluxes below $\sim 10^{-14}$ erg cm^{-2} s^{-1} in the hard band, the X-ray source population in these surveys is mainly composed of obscured AGN. This supports the suggestion by Setti & Woltjer (1989) that the spectral shape of the XRB is due to the integrated contribution of AGN affected by photoelectric obscuration with a wide range of gas column density (N_H) and redshifts. Since the resolved fraction of the XRB drops from $\approx 80-90\%$ at $2-6$ keV to $50-70\%$ at $6-10$ keV (Worsley et al. 2004), a sizable number of strongly absorbed AGN may still be missing in the X-ray surveys. An alternative method to detect heavily absorbed AGN is to select objects that have mid-IR and radio emission typical of AGN though faint near-IR and optical fluxes (Martinez-Sansigre et al. 2005). While this kind of study cannot quantify which fraction of these mid-IR selected, absorbed AGN would be detected by X-ray selection, the COSMOS survey (Scoville et al. 2007) will be able to answer this question due to its rich multi-wavelength coverage (from radio to X-ray) on a large area of the sky (2 deg^2).

The XMM-*Newton* wide-field survey in the COSMOS field (XMM-COSMOS, Hasinger et al. 2007), with an unprecedented combination of wide area coverage and high sensitivity, is providing a large number of

[1] Max Planck Institut für extraterrestrische Physik, Giessenbachstrasse 1, D–85748 Garching, Germany
[2] European Southern Observatory, Karl-Schwarzschild-Strasse 2, D–85748 Garching, Germany
[3] INAF-Osservatorio Astronomico di Bologna, via Ranzani 1, I–40127 Bologna, Italy
[4] Harvard-Smithsonian Center for Astrophysics, 60 Garden Street, Cambridge, MA 02138
[5] INAF-Osservatorio Astronomico di Roma, via Frascati 33, I-00040 Monteporzio Catone (Roma), Italy
[6] Laboratoire d'Astrophysique de Marseille, UMR 6110 CNRS-Université de Provence, BP8, 13376 Marseille Cedex 12, France
[7] Max Planck Institut für Astronomie, Königstuhl 17, Heidelberg, D-69117, Germany
[8] Steward Observatory, University of Arizona, 933 North Cherry Avenue, Tucson, AZ 85721
[9] Department of Physics, ETH Zurich, CH-8093 Zurich, Switzerland
[10] Department of Physics, Carnegie Mellon University, 5000 Forbes Avenue, Pittsburgh, PA 15213
[11] California Institute of Technology, MC 105-24, 1200 East California Boulevard, Pasadena, CA 91125
[12] Space Telescope Science Institute, 3700 SanMartin Drive, Baltimore, MD 21218
[13] Visiting Astronomer, Univ. Hawaii, 2680 Woodlawn Dr., Honolulu, HI, 96822
[14] Physics Department, Graduate School of Science & Engineering, Ehime University, Bunkyo-cho 2-5, Matsuyama, Ehime 790-8577, Japan

⋆ Based on observations obtained with XMM-*Newton*, an ESA science mission with instruments and contributions directly funded by ESA Member States and NASA

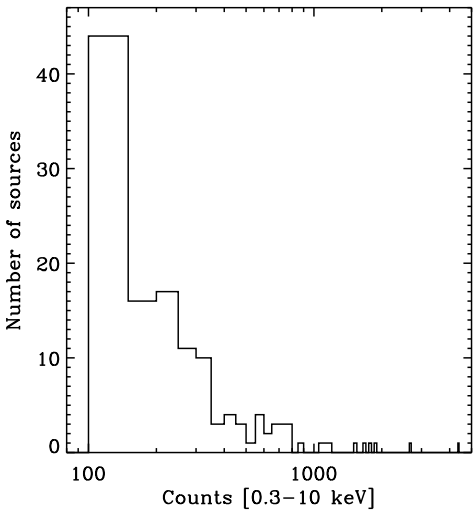

FIG. 1.— Net [0.3-10] keV *pn* counts distribution for the sample of 135 X-ray sources used in this work.

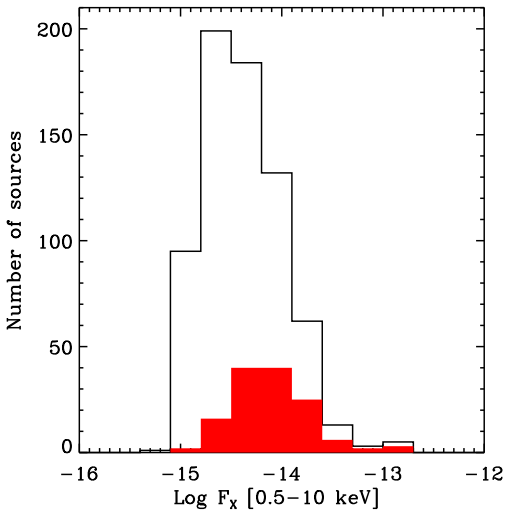

FIG. 2.— X-ray [0.5-10 keV] flux distribution for all the X-ray sources (empty histogram) and for the sample of spectroscopically identified sources (filled histogram), with more than 100 net counts, we analyze in this work.

AGN with enough counts to perform a detailed study of their X-ray spectra. This spectral information, particularly the N_H distribution, is a fundamental input parameter to model the XRB (e.g. Comastri et al. 1995; Gilli et al. 2001). While we anticipate the completion of the multi-wavelength campaigns including the optical spectroscopic follow-up within the next few years, we report in this paper the X-ray spectral fitting results for a preliminary sample of spectroscopically-identified X-ray sources. The paper is structured as follows: in §2 we describe the sample selected on the basis of counts statistics and optical identification; in §3 we describe our X-ray spectral extraction procedure, in §4 we present the results of the X-ray spectral analysis, in §5 we discuss the properties of four Type-2 QSOs, in §6 we compare the X-ray and optical classification, and finally we summarize our conclusions in §7.
Throughout the paper we assume $H_0 = 70$ km s^{-1} Mpc^{-1}, Ω_m=0.3 and Ω_Λ=0.7.

2. SAMPLE SELECTION

XMM-*Newton* has imaged the full 2 deg^2 of the COSMOS area down to the following flux limits in the respective energy bands: 7×10^{-16} erg cm^{-2} s^{-1} [0.5-2 keV], 4.0×10^{-15} erg cm^{-2} s^{-1} [2-10 keV] and 1.0×10^{-14} erg cm^{-2} s^{-1} [5-10 keV] (see Fig. 7 of Cappelluti et al. 2007 for details on the sky coverage as a function of the X-ray flux). A general outline of the survey can be found in Hasinger et al. (2007). Further details such as the point-source detection method and sky area coverage as a function of the X-ray flux are presented in Cappelluti et al. (2007). Our sample is based on the X-ray catalogue of 1390 point-like sources (Cappelluti et al. 2007). We limit our analysis to the sources detected with the EPIC pn−CCD (*pn*) camera (Strüder et al. 2001), in the first 12 XMM-COSMOS observations since optical spectroscopic follow-up (Trump et al. 2007; Lilly et al. 2007) has been concentrated in this area (~ 1.3 deg^2). These 12 fields are flagged in Table 1 of Hasinger et al. (2007). Reliable optical counterparts (Brusa et al. 2007) have been determined for $\sim$ 90% of the sources in these 12 fields. We exclude 20 of the 715 X-ray sources in this area that are classified as "extended" from the detection algorithm. The observed X–ray emission from these sources is likely to be due to a group or cluster of galaxies, while here we are interested in selecting AGN. From the remaining 695 X–ray sources, we select sources with greater than 100 net counts in the [0.3-10] keV energy band and optical spectroscopic identification. We further remove one source that has been identified as a star (Trump et al. 2007). The final sample comprises 135 objects. We show the distribution of their net counts in the [0.3-10] keV band in Figure 1 and the [0.5-10] keV flux distribution (Figure 2) that covers a range of 1.4×10^{-15}, 1.2×10^{-13} erg cm^{-2} s^{-1}. From their optical spectra, we can further subdivide our sample based on the presence of broad emission lines: *'Broad Line AGN'* (BL AGN, 86 objects; FWHM>2000 km s^{-1}), *'NON-Broad Line AGN'* (NON-BLAGN, 49 objects; FWHM<2000 km s^{-1}). We note that in this latter class there are objects showing clear signs of nuclear activity such as high excitation emission lines, as well as sources with normal galaxy spectra. We compare this purely optical classification with the X-ray properties of our sources in Sec. 6.

3. EXTRACTION OF X-RAY SPECTRAL PRODUCTS

We have implemented an automated procedure to produce the X-ray spectrum for each source by combining counts from individual exposures. We have used the latest release of the XMM-*Newton* Science Analysis System (SAS)[16] software package (v 7.0). The task *region* has been used to generate the source and background extraction regions. The source region is defined as a circle with radius r_s that varies according to the signal-to-noise and the off-axis angle of the detection to optimize the quality of the final spectrum. The radii of these regions are reduced by the task to avoid overlapping with the extraction regions of nearby sources. All source re-

[16] http://xmm.vilspa.esa.es/external/xmm_sw_cal/sas_frame.shtml

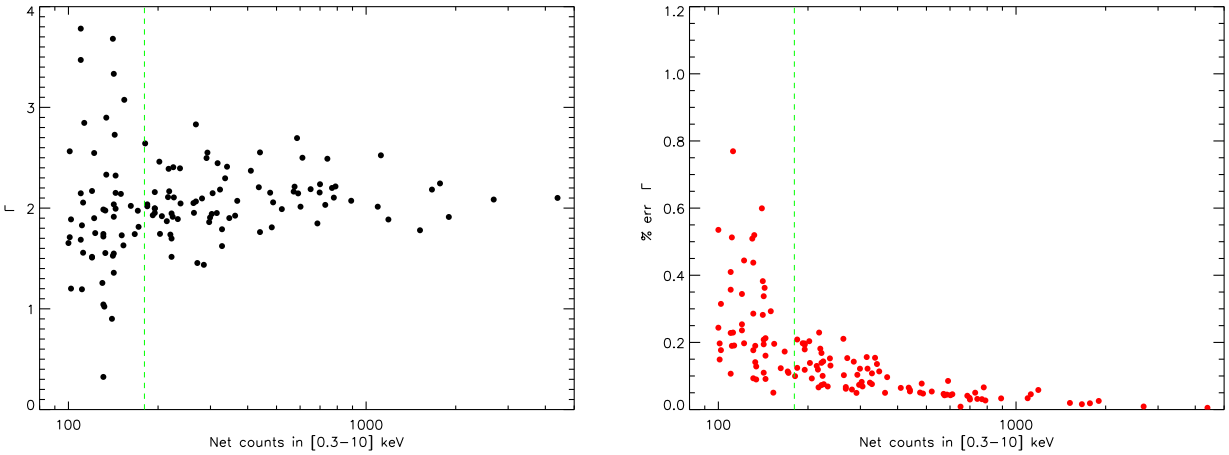

FIG. 3.— *Left*: spectral slope value (Γ) from the fit of each single source using the PL model as a function of the net counts in the full [0.3-10] keV band. *Right*: fractional statistical error (1σ) on Γ as a function of the net counts in the [0.3-10] keV energy band. The dashed line in both plots is the threshold of 180 net counts in the [0.3-10] keV band that divides the *bright* from the *faint* sample.

gions are further excised from the area used for the background measurement. The task *especget* has been used to extract from the event file the source and background spectra for each object. The same task generates the calibration matrices (i.e. arf and rmf) for each spectrum and determines the size of the source and background areas while updating the keyword BACKSCAL in the header of the spectra appropriately[17]. The single pointing spectra have been combined with *mathpha* to generate the spectrum of the whole observation.[18] For each source in our sample, we use all the available counts from the XMM-COSMOS observations, including those coming from overlapping fields not included in the 12 fields list (see Fig.1 Hasinger et al. 2007). Finally, in order to use the χ^2 minimization technique, we bin the spectra with *grppha* so that each bin has at least 20 counts.

4. SPECTRAL ANALYSIS

Tozzi et al. (2006) have shown by extensive simulations that below 50 counts the best fit values obtained using Cash statistics (Cash 1979) are more accurate than those obtained with the χ^2. For greater than 50 counts, the two methods give equivalent results. Since we limit our analysis in this paper to sources with more than 100 counts, we are confident that the results obtained with the χ^2 minimization technique are accurate. We use XSPEC[19] (v11.3.2p) for our spectral fitting analysis. We first fit the data with two basic input models: a simple *powerlaw* (*PL*) and a *powerlaw* modified by intrinsic absorption at the redshift of the source (*APL*). Both models include an additional component to account for photoelectric absorption due to the Galactic column density that is fixed to the value in the COSMOS region ($N_H^{Gal} \sim 2.7 \times 10^{20}$ cm^{-2}, Dickey & Lockman 1990)[20]. The PL model is made of two XSPEC components *wabs*zpowerlw*, while the APL model consists of the combination of three different components *wabs*zwabs*zpowerlw*. The *wabs* model describes the photoelectric absorption using Wisconsin cross-sections (Morrison & McCammon 1983) and its only parameter is the equivalent hydrogen column density (*zwabs* has the redshift as an additional parameter). *zpowerlw* is a simple power law parameterized by the photon index, the redshift and a normalization factor.[21] The model fits yield the power-law photon index Γ, the X-ray luminosity in the [0.5-2] and [2-10] keV rest-frame bands, and from the *APL* model also the intrinsic column density N_H . We notice that the dispersion of Γ for our sample increases significantly for sources with low counts statistics (Fig. 3, left panel) and in particular the fractional error becomes quite large (Fig. 3, right panel). Above 180 net counts, the fractional error remains below 20%. Hence, we split our sample in two: *sample-1* including 82 sources with more than 180 net counts, and *sample-2* having 53 sources with less than 180 counts. For *sample-1*, we allow both Γ and N_H free to vary, while we fix Γ to the average value, obtained with *sample-1*, for lower count sources (*sample-2*).

For all the 135 X-ray sources, we perform a spectral fit using both *PL* and *APL* models. We label a source as X-ray absorbed in those cases for which the *APL* model is a better fit, than the pure *PL*, with a confidence level threshold of 90% based on an F-test.

The output of our spectral analysis is reported in Tab. 4. The table has the following structure: IAU name (col.1), identification number (xid, col.2), X-ray coordinates (col.3-4), net detected X-ray counts in the [0.3-10] keV band (col. 5), spectroscopic redshift (col. 6), best fit model (col. 7), spectral index Γ (col. 8), intrinsic column density N_H (col. 9), X-ray fluxes (col. 10-11-12), de-absorbed X-ray luminosities (col. 13-14-15).

4.1. *Notes on some individual sources*

[17] The header keyword BACKSCAL is set to 1 for the source spectrum while for the background spectrum it is fixed to the ratio between the background to source areas.

[18] We note that all the XMM-Newton observations in the COSMOS field have been performed with the thin filter for the *pn* camera.

[19] http://heasarc.gsfc.nasa.gov/docs/xanadu/xspec/

[20] This is an average value for the Galactic N_H in the COSMOS area where N_H^{Gal} is in the range [2.5-2.9] $\times 10^{20}$ cm^{-2}. This range in Galactic column density does not affect the results of our spectral analysis.

[21] We refer the reader to http://heasarc.gsfc.nasa.gov/docs/xanadu/xspec/ for further details on the spectral models.

TABLE 1
Parameters of the best fit model for sources with soft excess

XID	counts[a]	Model[b]	$\chi^2/d.o.f.$	Γ[c]	N_H[d]	kT[e]	Γ[f]	Redshift	Opt. class[g]
41	315	APL+po	0.94	$1.72^{2.57}_{1.38}$	$21.38^{21.59}_{21.02}$		2.0	0.114	NLAGN
		APL+bb	0.83	$1.95^{2.37}_{1.65}$	$21.51^{21.55}_{20.42}$	30^{+2}_{-3}			
106	141	APL+po	0.25	2.0	$22.33^{22.66}_{21.98}$		2.0	0.710	gal
		APL+bb	0.26	2.0	$22.28^{23.00}_{21.96}$	121^{+914}_{-71}			
117	111	APL+po	0.69	2.0	$22.76^{23.14}_{22.37}$		2.0	0.936	gal
		APL+bb	0.59	2.0	$22.57^{22.86}_{20.42}$	81^{+48}_{-18}			
274	112	APL+po	0.26	2.0	$22.67^{23.00}_{22.18}$		2.0	0.677	gal
		APL+bb	0.24	2.0	$22.55^{23.00}_{20.42}$	124^{+878}_{-119}			

[a] Net *pn* counts in the [0.3-10] keV energy range.[b] Best fit model: APL+po=absorbed power-law plus an extra power-law for the soft excess; APL+bb=absorbed power-law plus a blackbody for the soft excess.[c] Slope of the powerlaw model (photon index).[d] Logarithm of the intrinsic absorption (cm^{-2}).[e] Temperature (in eV) of the blackbody used to model the soft excess.[f] Slope of the extra power-law used to model the soft excess.[g] Optical classification, see Sec. 6 for details.

For each source we carefully check the results obtained with the basic *PL* and *APL* models and, if significant residuals are present, we refine the fit using more complex models. We show in Fig. 4 a representative X-ray spectrum for each one of the different best-fit models. We use the F-test and a confidence level threshold of 90% to choose between the different models.

4.1.1. *Soft excess*

A clear *soft excess* is present in four of our sources (xid 41, 106, 117, 274). This feature, first observed with EXOSAT (Arnaud et al. 1985; Turner & Pounds 1989), has been confirmed by XMM-*Newton* observations (e.g. Pounds & Reeves 2002; Porquet et al. 2004; Gallo et al. 2006), but its origin is still uncertain. Such a soft component may be the high energy tail of the UV bump (a blackbody model is appropriate in this case), or can be due to reprocessed emission scattered along our line of sight by a photo-ionized gas located just above the obscuring torus (an additional power-law with the spectral index fixed to the value of the hard X-ray primary power-law is a good parameterization of this scenario). We fit these four sources adding to the basic APL model an extra component represented either by a power-law (*po*) or a blackbody (*bb*[22]) according to the two physical scenarios mentioned above. We report in Tab. 1 the parameters of the additional component in the fit of these four sources. We are not able to distinguish on a statistical basis between the two models given the similar values of χ^2. Nevertheless, we notice that all these four sources present intrinsic absorption and therefore we exclude that the soft-excess of these objects is due to the high energy tail of the UV bump (APL+bb).

4.1.2. *Fe Kα line*

Three sources show significant features ascribable to the redshifted Fe Kα emission line: xid 2028, 2043, 2608. For these sources we add a Gaussian component (*gauss*) to the model, fixing the line energy to $6.4/(1+z)$ keV. The best fit values of interesting parameters are reported in Tab. 2. We show in Fig. 5 the ratio of the data versus the model (powerlaw for xid 2028, 2043 and pexrav[23] for xid 2608) in an energy range around the expected location of the Fe Kα line. Interestingly all three of these sources do not show sign of AGN activity from their optical spectra and are therefore classified as 'galaxy'.

TABLE 2
Parameters of the *gauss* additional component for the sources with Fe line

XID	σ[a]	EW[b]	Redshift	Opt. class[c]
2028	616^{+364}_{-224}	2754^{+1628}_{-1002}	0.784	gal
2043	179^{+120}_{-115}	748^{+502}_{-481}	0.668	gal
2608	281^{+408}_{-175}	792^{+1151}_{-493}	0.125	gal

[a] Observed width of the line in eV.[b] Rest frame equivalent width of the line in eV[c] Optical classification, see Sec. 6 for details.

4.1.3. *Thermal emission?*

Source xid 54, if fitted with an APL model, gives a large value for the spectral slope ($\Gamma > 3$) and significant residuals in the 0.3-10 keV energy range. An alternative description of its spectrum is obtained assuming we are observing thermal emission, parameterized with a Raymond-Smith model (Raymond & Smith 1977) with a temperature kT= $1.6^{+0.4}_{-0.2}$ keV fixing the metalicity to 0.3 solar. Source xid 54 is identified with two interacting galaxies (see Fig. 6) at redshift z= 0.350 with no sign of AGN activity from its optical spectrum. Its X-ray luminosity of 3×10^{42} erg s^{-1} is larger than that expected for early-type galaxies (Matsushita et al. 2001) and, from the optical imaging, there is a concentration of galaxies around xid 54 with the same photometric redshifts therefore supporting the idea that we are looking at the X-ray emission from a group of galaxies. Nevertheless, we can not exclude with the current data that a fraction of the X-ray flux of source 54 could come from an absorbed nucleus (e.g XBONGS, Comastri et al. 2002) or from discrete sources like LMXBs or HMXBs in the galaxy. A Chandra observation with its higher angular resolution could possibly locate discrete sources inside xid 54.

4.1.4. *XID=2608 : a Compton-thick AGN?*

[22] This is a blackbody spectrum defined by the temperature kT in keV and a normalization factor.

[23] An exponentially cut off power law spectrum reflected from neutral material. We refer the reader to Magdziarz & Zdziarski (1995) for a detailed description of such model.

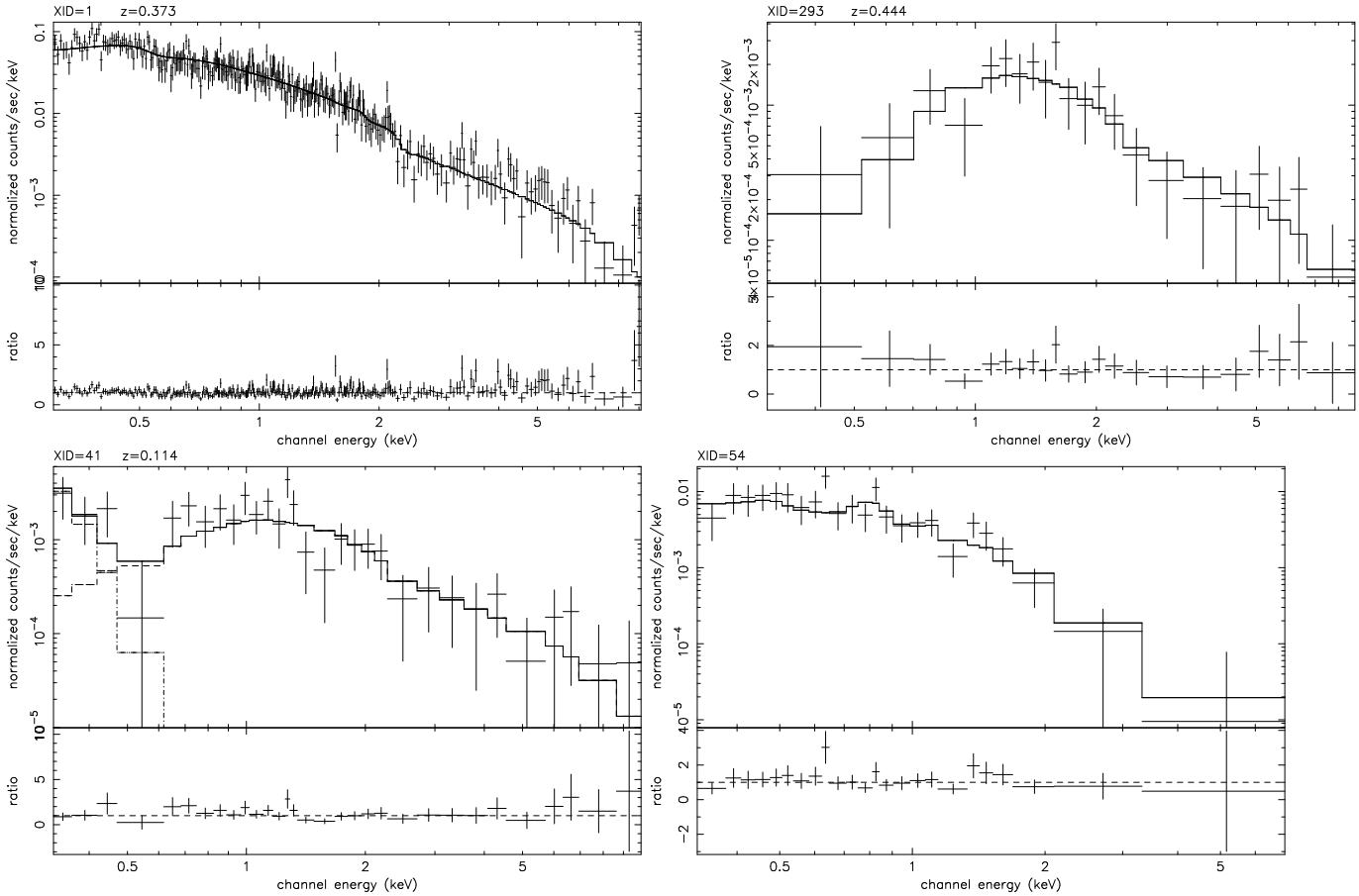

FIG. 4.— Examples of X-ray spectra with different best fit model. *Top-left*: unabsorbed power-law (PL); *top-right*: absorbed power-law (APL); *bottom-left*: absorbed power-law plus a black-body component to model the soft excess; *bottom-right*: thermal emission parameterized with a Raymond-Smith model.

An additional source that requires a more complex modeling of its spectrum is xid 2608. The fit with the APL model gives an extremely flat value for Γ (≈ 0.3) and large residuals at both low and high energies (see left panel of Fig. 7). Hasinger et al. (2007) found that this source is located in an area populated by local Compton-thick Seyfert-2 galaxies in an X-ray color-color diagram (see Fig. 12 of Guainazzi et al. 2005). This, together with other evidences based on lines ratios from the optical spectrum, supports the hypothesis that source 2608 is a heavily absorbed AGN.

We use the 131 net counts from the pn camera for this source to study more in detail its X-ray spectrum. A pure reflection component model (*pexrav*) is a better description compared to the APL model according to an F-test with a confidence level of 95%. Nevertheless this fit leaves a clear residual around the expected position of the 6.4 keV Fe Kα line. The best-fit model for xid 2608 is a pure reflection model plus a Gaussian line at 6.4 keV rest-frame (*pexrav + gauss*). The details for the different spectral fits are reported in Tab. 3. The presence of the Fe Kα fluorescent line at 6.4 keV is significant at 95% according to an F-test. The presence of the line is a clear sign that the source is heavily absorbed, but a useful observable to confirm its Compton-thick nature is the Equivalent Width (EW) of the same line. The nominal best fit value for the EW (792^{+1151}_{-493} eV) is higher than the maximum (600 eV) observed EW in Compton-thin objects (Turner et al. 1997). This supports the idea that source 2608 is a Compton-thick AGN, although we have to mention that with the current photons statistics, the error for the observed flux of the line (and consequently for the EW) is still large. We are confident that an improved result will come after the completion of the additional 600 ksec XMM observations awarded in AO4. Another diagnostic on the Compton-thick nature of this source could be the *thickness parameter* T=F[2-10keV]/F[OIII]. A high quality optical spectrum for this source is available in the Sloan Digital Sky Survey archive and we obtain a value for F[OIII] from the analysis of Kauffmann et al. (2003). The [OIII] flux has been corrected for the extinction toward the narrow-line region as deduced from the Balmer decrement. We obtain T= 3.8 which is in a "grey area" where both Compton thick and less absorbed AGN are located (see for example Fig. 1 of Bassani et al. 1999).

In Fig. 13, we assume as a lower limit for the column density of xid 2608 the value 1.5×10^{24} cm^{-2} where the Compton optical depth is equal to unity and the directly transmitted nuclear emission is strongly suppressed in the [0.3-10] keV band. For the luminosity of this object, if we assume that only 3% of the flux has been reflected, we obtain a value of $\sim 7.4 \times 10^{43}$ erg s^{-1}, while for reflected fractions between $10-1$% the luminosity would be in the range $(0.2 - 2.2) \times 10^{44}$ erg s^{-1}.

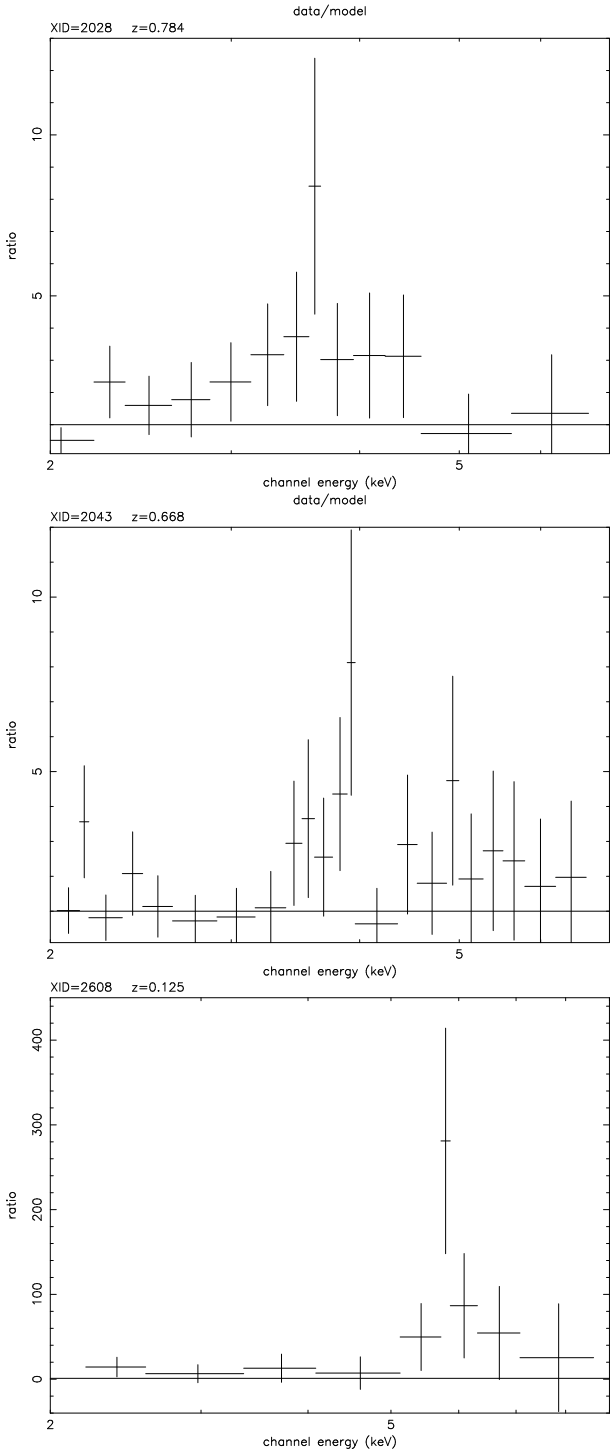

FIG. 5.— The ratio of the data versus a powerlaw model (top panels) or a pexrav model (bottom figure) around the energy of the Fe Kα line for the three sources with significant detection of this feature.

4.2. *Spectral properties of the sample*

As mentioned in Sec. 4, we leave both Γ and N_H free to vary when fitting the sources in *sample-1*. The results of this analysis are summarized in Fig. 8. The average value of Γ does not change as a function of N_H as already noticed in deep surveys (i.e. Mainieri et al. 2002). We obtain, using the weighted mean, $< \Gamma >= 2.06 \pm 0.08$ and the observed dispersion of the distribution of the best fit values is $\sigma \approx 0.25$. As the typical error in a single measurement of Γ is $\Delta\Gamma = 0.09$, assuming that both statistical errors and the intrinsic dispersion are distributed as a Gaussian, the intrinsic scatter in Γ is $\sigma_{int} \sim 0.24$. For comparison with X-ray spectral studies in a similar X-ray flux range of our sample, Mateos et al. (2005a) from a large sample of serendipitous sources detected with XMM-*Newton* in a $\sim$ 3.5 deg^2 area, obtained $< \Gamma >= 1.96 \pm 0.01$; Perola et al. (2004) in the spectroscopic analysis of the HELLAS2XMM 1df found $< \Gamma >= 1.90 \pm 0.22$; Page et al. (2006) from the spectral fit of AGN in the 13^H XMM-*Newton*/Chandra deep field found $< \Gamma >= 2.0 \pm 0.1$ with an intrinsic dispersion $\sigma \approx 0.36$. All these measurements are consistent with each other within the uncertainties. Adopting the optical classification described in Sec. 2 the mean value for the spectral slope for BLAGN (58 sources) is $< \Gamma >= 2.09$ with a dispersion of $\sigma \approx 0.26$, while for not BLAGN (24 sources) we obtain $< \Gamma >= 1.93$ and $\sigma \approx 0.29$. Furthermore, we confirm that the average value of the photon index does not vary with redshift in the range z=[0.0,3.0] covered by our sample, thus confirming previous findings (e.g. see Fig. 9 of Piconcelli et al. (2003) for a compilation from the literature)

The other physical quantity that we measure from the spectral fitting is the column density N_H. In this case, we consider all our 135 sources since N_H has been left

TABLE 3
PARAMETERS OF THE BEST FIT MODEL FOR SOURCE XID 2608

Model[a]	Γ	N_H[b]	EW[c]	χ^2	d.o.f.
APL	2.0	$0.16^{+0.75}_{-0.16}$		9.3	11
pexrav	2.0			4.1	9
pexrav+gauss	2.0		792^{+1151}_{-493}	1.7	7

[a] Best fit model: *APL* = absorbed power-law; *pexrav* = pure reflection model; *pexrav+gauss* = pure reflection model plus a Gaussian line.[b] Hydrogen column density in unit of 10^{22} cm^{-2}.[c] Equivalent width of the Fe Kα line expressed in eV.

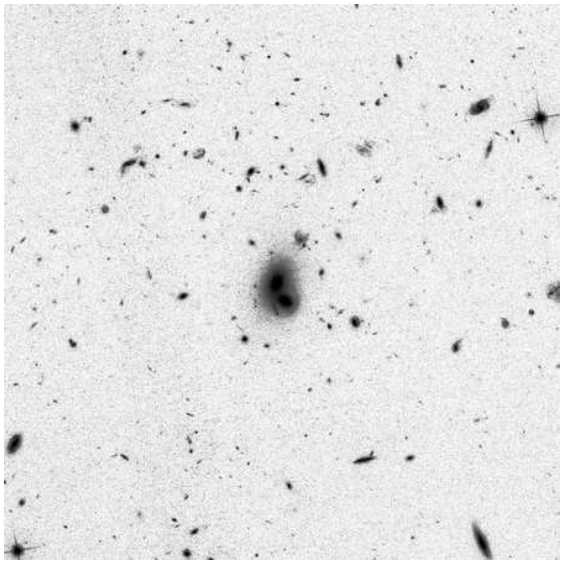

FIG. 6.— ACS image of source xid 54. The cutout is 90 arcsec on a side.

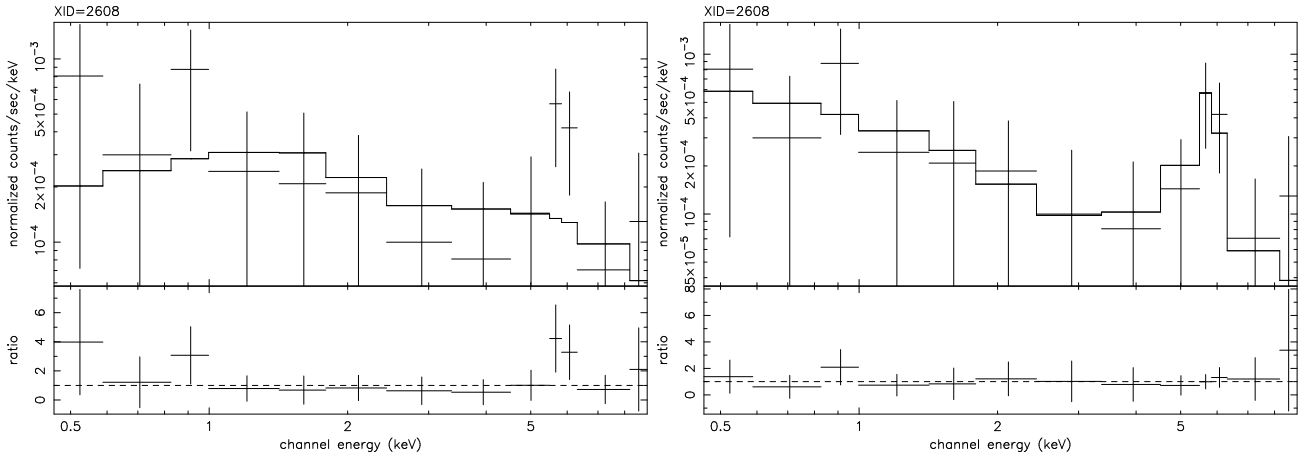

FIG. 7.— The X-ray fit of source xid 2608 with the basic APL model (*left*) and a pure reflection model plus a Gaussian line (*right*).

free to vary both in *sample-1* and *sample-2*. According to an F-test, 32 X-ray sources do require intrinsic absorption in excess to the Galactic one, at a confidence level larger than 90%. Therefore a fraction as large as 24% of our sample is made of X-ray absorbed AGN. Fig. 9 shows the distribution of N_H values for these sources. We note that the observed N_H distribution refers only to the sources inside the region in the N_H-L_X-z space delimited by the count-rate detection threshold of our survey. This introduces a bias against absorbed sources, and therefore the fraction of absorbed sources detected in our study has to be considered a lower limit. According to the most recent population synthesis model of the XRB (Gilli et al. 2006), in the band used to select our sample the expected fraction of obscured source with column density $N_H > 10^{21}$ cm^{-2} is 20% that is consistent with what we found. In Fig. 9 we divide BL AGN from NOT BL AGN. The visual impression that NOT BL AGN have larger column densities than BL AGN is confirmed by a Kolmogorov-Smirnov test that gives a probability larger than 99.9% that the two distributions are different. No object with $N_H > 10^{22}$ cm^{-2} shows broad lines in its optical spectrum. Nevertheless, 9% (8/86) of the BL AGN in our sample do show some intrinsic absorption in their X-ray spectra (see also Mittaz et al. 1999; Fiore et al. 2001; Page et al. 2001; Schartel et al. 2001; Tozzi et al. 2001; Mainieri et al. 2002; Brusa et al. 2003; Perola et al. 2004; Mateos et al. 2005b).

In Fig 10 we show the distributions of the R-K (Vega) colors for the sources with 'PL' as best fit model (empty histogram) and for the ones that instead require an absorbed power-law (hatched histogram). The two distributions are significantly different according to a Kolmogorov-Smirnov test with a probability of 99.99%. The X-ray sources that require an absorption component in their spectral fit are on average redder, suggesting a correlation between X-ray absorption and optical to near-IR colors. On the contrary, sources that do not show absorption in their X-ray spectra have bluer color typical of optically selected, unobscured quasars. These results confirm those obtained from an analysis based on HR values made by Brusa et al. (2007) (see their Fig. 10). Nevertheless the interpretation of this correlation between X-ray absorption and optical to near-IR colors is not straightforward since we are sampling different scales in the two measurements (i.e. nucleus with the X-ray data and nucleus+host galaxy with the R-K colors).

When the number of counts in a source is inadequate to perform a spectral fit, a widely used tool to study the general spectral properties of an X-ray source is the hardness ratio $HR = (H - S)/(H + S)$, where H are the counts in the [2-4.5] keV band and S those in the [0.5-2] keV energy band. In Fig. 11 we show the hardness ratio values versus the amount of intrinsic absorption derived from our spectral analysis (both *sample-1* and *sample-2*). A clear correlation between the two quantities is present: 90%[24] of the sources with $N_H > 10^{22}$ cm^{-2} have HR> -0.3 and 99% of the sources with $N_H < 10^{22}$ cm^{-2} have HR< -0.3. Therefore, although one has to remember that the HR is a strong function of redshift (e.g. Fig. 8 in Szokoly et al. 2004), it is still possible to use HR for statistical studies.

Another diagnostic that can yield important information on the nature of X-ray sources is the X-ray-to–optical flux ratio (e.g., Maccacaro et al. 1988; Stocke et al. 1991). The majority of the AGN have X-ray-to-optical flux ratios (X/O) of 0.1 $<$X/O$<$ 10 (e.g., Akiyama et al. 2000; Lehmann et al. 2001), but *Chandra* and XMM-*Newton* surveys have shown that there is a non negligible population of AGN with high X/O (> 10) and that a large fraction of them are obscured, and possibly high-redshift, Type-2 QSOs (e.g., Fabian et al. 2000; Mainieri et al. 2002; Fiore et al. 2003; Mignoli et al. 2004; Mainieri et al. 2005). For comparison with the literature, we define X/O as the ratio between the X-ray flux in the [2-10] keV band and the flux in the optical R band. In Fig. 12 we plot the X/O values for the sources in our sample versus the N_H. Out of the seven sources that have X/O> 10, four show absorption in their X-ray spectra (APL) and one is a Type-2 QSO. We notice that the other three Type-2 QSO candidates in our sample (see Sec. 5) have X/O values inside the range 0.1 $<$X/O$<$ 10 where most of the optical or soft X-ray selected AGN are located. Since we limit our analysis to the brighter X-ray sources and the spectroscopic follow-up is not complete, we postpone any further analysis on the nature of X/O> 10 sources to a future paper.

[24] We note that the only source with $N_H > 10^{22}$ cm^{-2} and HR< -0.3 shows a soft excess in its X-ray spectrum.

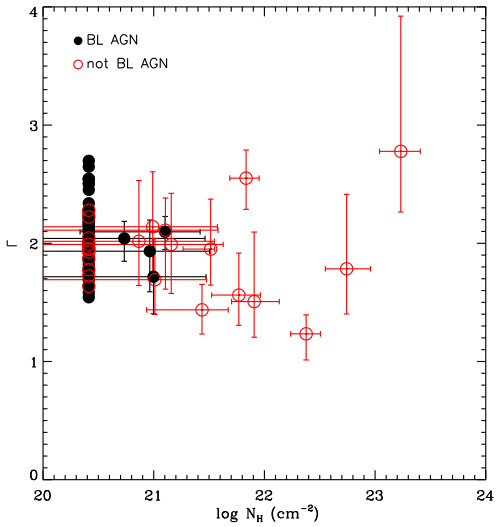

FIG. 8.— Γ versus N_H for the X-ray sources with more than 180 net counts in [0.3-10] keV (bright sample) and spectroscopically identified. Filled circles are BL AGN, while empty circles are not BL AGN. Error bars correspond to 1σ. To simplify the figure, we did not report the error bars on Γ for unabsorbed sources and plotted them to N_H=$N_H^{gal} \approx 2.7 \times 10^{20}$ cm^{-2}.

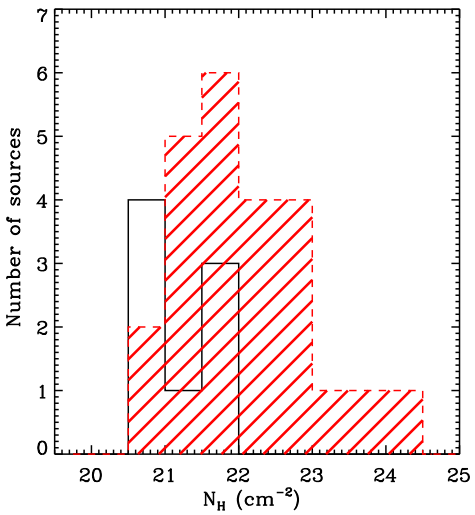

FIG. 9.— Intrinsic column density (N_H) distribution for BL AGN (empty histogram) and NOT BL AGN (hatched histogram) with intrinsic absorption in excess of the Galactic column density.

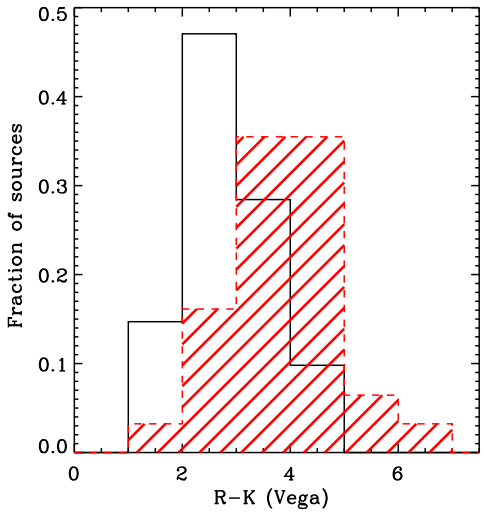

FIG. 10.— R-K colors (Vega) distribution for sources with PL as best fit model (empty histogram) and for sources with 'APL' as a best fit model (hatched histogram).

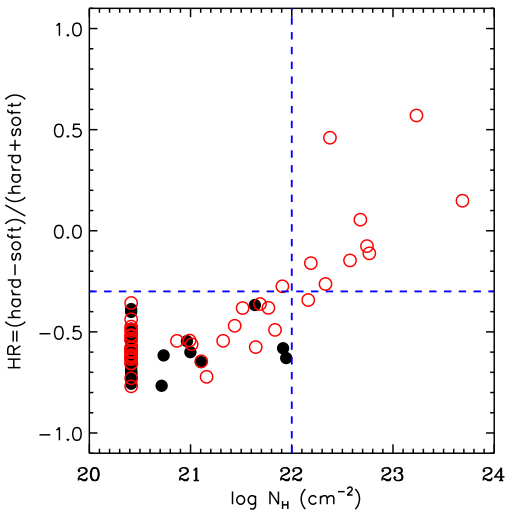

FIG. 11.— HR defined using the [0.5-2] (soft) and [2-10] (hard) bands versus the column density derived from the spectral fitting analysis. Only sources with errors on the HR smaller than 0.3 have been plotted. Filled circles are BL AGN, while empty circles are NOT BL AGN. The horizontal dashed line corresponds to HR= −0.3 used to separate absorbed and unabsorbed sources, while the vertical dashed line indicates a column density equal to 10^{22} cm^{-2}.

5. TYPE-2 QSO CANDIDATES

Using the spectral parameters from the best-fit model, we correct the X-ray luminosity of each source for the intrinsic and Galactic absorption. These corrected luminosities are plotted in Fig. 13 versus the N_H for all the sources in our sample. Four objects are characterized by a high X-ray luminosity ($L_X[0.5-10\ keV] > 10^{44}$ erg s^{-1}) and substantial absorption ($N_H > 10^{22}$ cm^{-2}) and we can therefore classify them as Type-2 QSOs. Radio-loud Type-2 QSOs are known since long times thanks to radio surveys (see McCarthy 1993 for a comprehensive review), while radio-quiet Type-2 QSOs have been observed only recently in *Chandra* and XMM-*Newton* X-ray surveys (Dawson et al. 2001; Norman et al. 2002; Mainieri et al. 2002; Stern et al. 2002; Della Ceca et al. 2003; Fiore et al. 2003; Tozzi et al. 2006) and optical surveys (SDSS, Zakamska et al. 2003). Two of our Type-2 QSOs candidates, xid= 70, 2289, are clearly detected in the radio at 20 cm using the Very Large Array (VLA) with an integrated flux of 540 ± 24 and 52 ± 11 microJy respectively (Schinnerer et al. 2007). The radio power of these two sources is therefore $P_{1.4GHz} = 9.8 \times 10^{23}$ and 1.5×10^{23} W/Hz. Historically such radio power has been used to divide radio loud and radio quiet AGN but such a dividing line appears to be redshift dependent: $\approx 5 \times 10^{23}$ W/Hz for the Palomar Green sample (mainly below $z < 0.3$) up to 5×10^{25} W/Hz for the Large Bright Quasar Survey sample ($< z > \sim 1.2$). Since

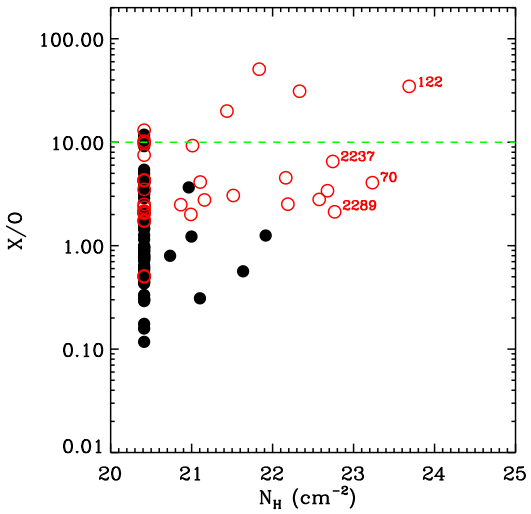

FIG. 12.— X/O (f[2-10 keV]/F(R)) versus N_H values. The filled circles are BL AGN, the empty circles NOT BL AGN. We label the four Type-2 QSOs candidates. The horizontal dashed line indicates the value X/O=10.

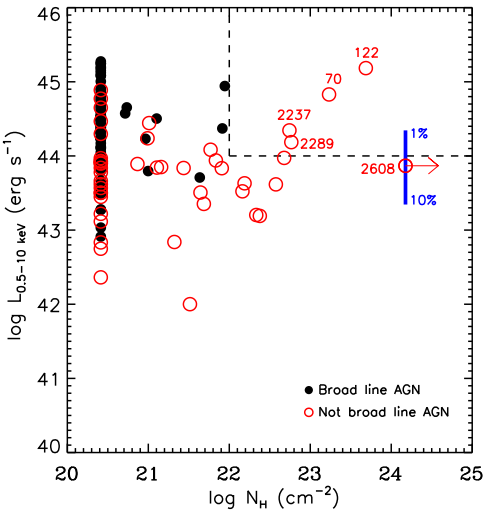

FIG. 13.— Intrinsic, de-absorbed X-ray luminosity in the [0.5-10] keV band vs. N_H. The filled symbols are BLAGN, while the empty symbols are not BLAGN. For source xid 2608 we assume a lower limit on N_H of 1.5×10^{24} cm^{-2} and for the luminosity we estimate a value of $\sim 7.4 \times 10^{43}$ erg s^{-1} assuming that a fraction of 3% is reflected (the error bar shows the luminosity range covered assuming that the reflected fraction is between 1% and 10%). See Sec. 4.1.4 for details. The dashed lines define the "Type-2 QSO region".

our two sources are at z$\sim 0.7-0.8$, we suggest to classify them as radio quiet AGN. The other two objects (xid= 122, 2237) are not detected in the radio and we can fix a 4.5 σ upper limit to their radio flux of 50 and 54 microJy (Schinnerer et al. 2007).
The optical spectra of these four sources show high excitation emission lines and their redshifts are 0.688, 0.831, 0.941, 2.418 respectively for xid 70, 2289, 2237, 122.
Using the multi-band photometry available from the COSMOS survey (Capak et al. 2007), we have derived the spectral energy distribution (SED) for the four Type-2 QSOs and compared them with the spectrum of NGC6240 and a Seyfert-2 composite spectrum derived from a sample of local galaxies by Schmitt et al. (1997) and Moran et al. (2001). While the SED of NGC6240 does not reproduce well the observed photometry of our Type-2 QSOs, an excellent description of the same is given by the composite Seyfert-2 SED (see right panels in Fig. 14). Furthermore, the R-K colors of these four objects are red (R-K=4.58, 3.91, 4.97, 4.76 respectively) although they can not be classified as EROs (R-K>5).

6. COMPARISON BETWEEN X-RAY AND OPTICAL CLASSIFICATIONS.

A classification based on the properties of the optical spectra of the 135 sources in our sample divides them into *'Broad Line AGN'* (BLAGN, 86 objects) if emission lines broader than 2000 km s^{-1} are present, *'Narrow Line AGN'* (NLAGN, 32 objects) if the optical spectrum shows high excitation emission lines and *'galaxy'* (gal, 17 objects) if there is no sign of AGN activity from the optical spectrum. As shown by deep *Chandra* and XMM-*Newton* surveys (e.g. Szokoly et al. 2004) a pure optical classification of AGN is biased against absorbed sources that appear as normal galaxies at those wavelengths. As previously done by Szokoly et al. (2004) and Tozzi et al. (2006), we introduce an X-ray based classification: we define *X-ray absorbed* AGN sources that are best fitted by an APL model compared to the PL one and have $L_X > 10^{42}$ erg s^{-1}, *X-ray unabsorbed* AGN sources best fitted with a PL model and $L_X > 10^{42}$ erg s^{-1} and finally *X-ray galaxies* sources with $L_X < 10^{42}$ erg s^{-1}.
Table 5 shows the comparison of the optical and X-ray classifications for our 135 sources. Ninety-one of these sources ($\sim$ 67%) have a similar classification from the optical and X-ray data. The best agreement between the two classifications is for Broad Line AGN (optical) and X-ray unabsorbed AGN (X-ray) for which the fractions of similar classifications are of the order of 91% (78/86 Broad Line AGN) and 76% (78/102 X-ray unabsorbed AGN) respectively. The $\sim$ 9% of BL AGN that show X-ray absorption in their X-ray spectra have values of the column density N_H below 10^{22} cm^{-2} (see empty histogram in Fig. 9). The main difference is instead for objects classified as galaxies on the basis of the optical spectra. Most of these objects (16/17) are classified as AGN (11 absorbed and 5 unabsorbed) on the basis of the X-ray luminosity. This confirms that the X-ray classification is more successful than the optical one in revealing the presence of black hole activity. The situation is intermediate for Narrow Line and X-ray absorbed AGN: only $\sim$ 41% of the optically classified Narrow Line AGN do show detectable X-ray absorption. We note that of the remaining Narrow Line AGN, $\sim$ 80% have z>0.4 and therefore the Hα line is outside the observed wavelength range, while for nine of them the MgII line is inside the observed range (i.e. $0.92 < z < 2.29$) but the S/N of the spectra could not be sufficient to detect a weak broad line. It is therefore possible that at least part of the disagreement between the optical and the X-ray classifications for these objects is due to less than optimal optical spectra, in terms of either spectral coverage or S/N.

7. CONCLUSIONS

We have presented the detailed spectral analysis of 135 X-ray sources from the XMM-*Newton* wide-field survey

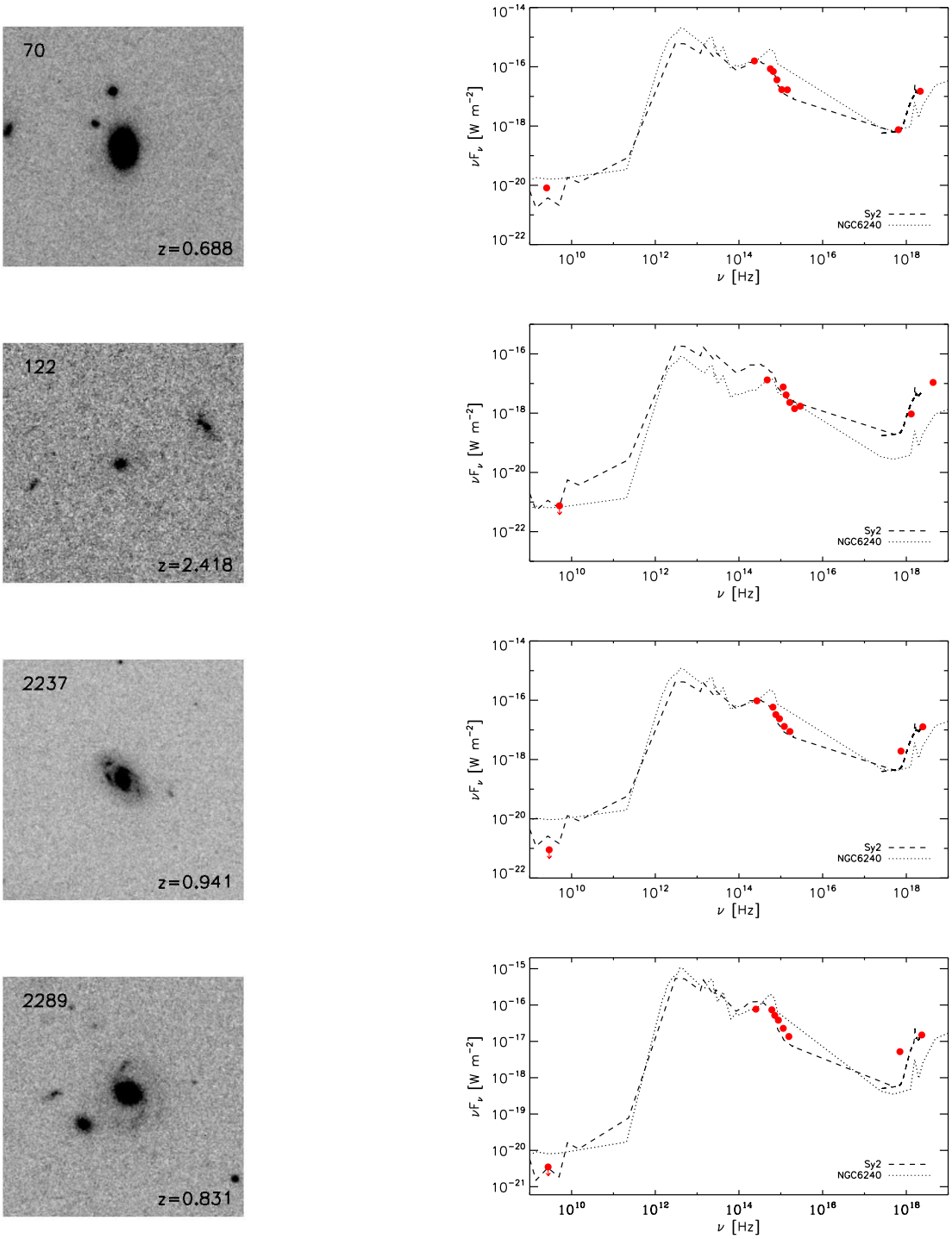

FIG. 14.— *Left*: *i*-band (F775W) ACS cutouts for the four Type-2 QSO candidates. Each cutout is 10 arcsec across. *Right*: the spectral energy distribution of the Type-2 QSO candidates (filled circles) compared to the SED of a composite Seyfert-2 spectrum (dashed line) and NGC6240 (dotted line).

in the COSMOS field. All the sources in our sample have more than 100 net counts in the [0.3-10] keV energy band and have been spectroscopically identified. For each source we have performed an accurate spectral fit in order to measure the continuum shape, the amount of absorbing matter and the strength of other spectral features. Our main results are summarized as follows:

- We find that, to the X-ray flux limit we are sampling ($F_X[0.5-10] = 1.4 \times 10^{-15}$ erg cm^{-2} s^{-1}), $\sim$ 76% of the spectra are well reproduced with a single power-law model, $\sim$ 20% require an absorbed power-law model and the remaining $\sim$ 4% need more complex models.

- The average value of the spectral slope of the intrinsic spectrum for the 82 sources with more than 180 net counts (*Sample-1*) is $< \Gamma >= 2.06 \pm 0.08$

with an intrinsic dispersion of $\sigma_{int} = 0.24$.

- We find no correlation between the spectral slope Γ and the amount of intrinsic absorption N_H, confirming that the hardening of the X-ray spectra going to fainter X-ray fluxes is due to the increased fraction of absorbed X-ray sources.

- None of the X-ray sources with a column density $N_H > 10^{22}$ cm^{-2} shows broad line in their optical spectra, although a fraction (9%) of broad line AGN shows intrinsic absorption in excess to the Galactic value.

- We detect (at more than 90% confidence level) the Fe Kα line in three objects. One of them is well described by a pure reflection model plus a Gaussian line at 6.4 keV rest-frame. This, the large equivalent width of the Fe line (although with large uncertainties) and diagnostics based on lines ratios from the optical spectrum support the hypothesis that this particular source is a Compton thick AGN.

- We find four radio-quiet Type-2 QSOs. Their spectral energy distribution is well reproduced with a Seyfert-2 composite spectrum.

- We confirm that in order to have a less biased sample of AGN it is crucial to complement the optical spectral properties with the X-ray informations (L_X and N_H), since many apparently normal galaxies in the optical band are instead absorbed AGN.

This is the first work on the X-ray spectral properties of the AGN in the COSMOS survey. We remark that once the XMM-*Newton* observations will be completed and the planned spectroscopic follow-up finished, we will be able to analyze the X-ray spectral properties of the AGN on a much larger sample and compare them with the properties of the AGN/host-galaxies at almost all the wavelengths.

This work is based on observations obtained with XMM–*Newton*, an ESA science mission with instruments and contributions directly funded by ESA Member States and the US (NASA). In Germany, the XMM-Newton project is supported by the Bundesministerium fr Wirtschaft und Technologie/Deutsches Zentrum fr Luft- und Raumfahrt (BMWI/DLR, FKZ 50 OX 0001), the Max-Planck Society and the Heidenhain-Stiftung. Part of this work was supported by the Deutsches Zentrum für Luft– und Raumfahrt, DLR project numbers 50 OR 0207 and 50 OR 0405. In Italy, the XMM-COSMOS project is supported by INAF and MIUR under grants PRIN/270/2003 and Cofin-03-02-23. We acknowledge financial contribution from contract ASI-INAF I/023/05/0. Based on observations with the NASA/ESA *Hubble Space Telescope*, obtained at the Space Telescope Science Institute, which is operated by AURA Inc, under NASA contract NAS 5-26555. The HST COSMOS Treasury program was supported through NASA grant HST-GO-09822. Also based on data collected at : the Subaru Telescope, which is operated by the National Astronomical Observatory of Japan; the European Southern Observatory under Large Program 175.A-0839, Chile; the National Radio Astronomy Observatory which is a facility of the National Science Foundation operated under cooperative agreement by Associated Universities, Inc.
We are grateful to Paolo Tozzi, Kazushi Iwasawa and Paolo Padovani for inspiring discussions. We gratefully acknowledge the entire COSMOS collaboration consisting of more than 70 scientists. More information on the COSMOS survey is available at
`http://www.astro.caltech.edu/$\sim$cosmos`. It is a pleasure the acknowledge the excellent services provided by the NASA IPAC/IRSA staff (Anastasia Laity, Anastasia Alexov, Bruce Berriman and John Good) in providing online archive and server capabilities for the COSMOS datasets.

REFERENCES

Akiyama, M. et al. 2000, ApJ, 532, 700
Alexander, D.M. et al. 2003, AJ, 126, 539
Arnaud, K.A. et al. 1985, MNRAS, 53, 197
Bassani, L. et al. 1999, ApJS, 121, 473
Brandt, W.N. et al. 2001, AJ, 122, 2810
Brusa, M. et al. 2003, A&A, 409, 65
Brusa, M. et al. 2007, ApJS, this volume
Capak, P. et al. 2007, ApJS, this volume
Cappelluti, N. et al. 2007, ApJS, this volume
Cash, W. 1979, ApJ, 228, 939
Comastri, A. et al. 1995, A&A, 296, 1
Comastri, A. et al. 2002, ApJ, 571, 771
Cowie, L.L. et al. 2002, ApJ, 566, L5
Dawson, S. et al. 2001, AJ, 122, 598
Della Ceca, R. et al.2003, A&A, 406, 555
Dickey, J.M. & Lockman, F.J. 1990, ARA&A, 28, 215
Fabian, A.C. et al. 2000, MNRAS, 315, L8
Finoguenov, A. et al. 2007, ApJS, this volume
Fiore, F. et al. 2001, MNRAS, 327, 771
Fiore, F. et al. 2003, A&A, 409, 79
Gallo, L.C., Lehmann, I., Pietsch, W. et al. 2006, MNRAS, 365, 688
Gilli, R. et al. 2001, A&A, 366, 407
Gilli, R., Comastri, A., Hasinger, G. 2006, A&A in press [astro-ph/0610939]
Guainazzi, M., Matt, G., Perola, G.C., 2005, A&A, 444, 119
Hasinger, G. et al. 1998, A&A, 329, 482
Hasinger, G. et al. 2001, A&A, 365, L45
Hasinger, G. et al. 2007, ApJS, this volume
Kauffmann, G. et al. 2003, MNRAS, 346, 1055
Koekemoer, A.M. et al. 2007, ApJS,this volume
Lehmann, I. et al. 2001, A&A, 371, 833
Leauthaud, A. et al. 2007, ApJS,this volume
Lilly, S. et al. 2007, ApJS, this volume
Loaring, N.S. et al. 2005, MNRAS, 362, 1371
Maccacaro, T. et al. 1988, ApJ, 326, 680
Magdziarz, P. & Zdziarski. A.A., 1995, MNRAS, 273, 837
Mainieri, V. et al. 2002, A&A, 393, 425
Mainieri, V. et al. 2005, A&A, 437, 805
Marleau, F.R. & Simard, L. 1998, ApJ, 507, 585
Martinez-Sansigre, A. et al. 2005, Nature, 436, 666
Mateos, S. et al. 2005a, A&A, 433, 855
Mateos, S. et al. 2005b, A&A, 444, 79
Matsushita, K. et al. 2001, ApJ, 547, 693
McCarthy, P.J. et al. 1993, ARA&A, 31, 639
Mignoli, M. et al. 2004, A&A, 418, 827
Mittaz, J.P.D. et al. 1999, MNRAS, 308, 233
Moran, E.C. et al. 2001, AJ, 556, L75
Morrison, R. & McCammon, D. 2001, AJ, 556, L75
Norman, C. et al. 2002, ApJ, 571, 218
Page, M.J.. et al. 2001, MNRAS, 325, 575
Page, M.J.. et al. 2006, MNRAR in press, [astro-ph/0604015]
Perola, G.C. et al. 2004, A&A, 421, 491
Piconcelli, E. et al. 2003, A&A, 412, 689
Pounds, K. & Reeves, J. 2002, 'New Visions of the X-ray Universe in the XMM-Newton and Chandra Era', [astro-ph/0201436]
Porquet, D. et al. 2004, A&A, 422, 85
Raymond, J.C. & Smith B.W. 1977, ApJS, 35, 419
Rosati, P. et al. 2002, ApJ, 566, 667
Schartel, N. et al. 2001, A&A, 320, 696

Schinnerer, E. et al. 2007, ApJS, this volume
Schmitt, H.R. et al. 1997, AJ, 114, 592
Scoville, N.Z. et al. 2007, ApJS, this volume
Setti, G. & Woltjer, L. 1989, A&A, 224, L21
Simard, L. 1998, ASPC, 145, 108S
Stern, D. et al. 2002, ApJ, 568, 71
Stocke, J.T. et al. 1991, ApJS, 76, 813
Strüder, L. et al. 2001, A&A, 365, 18
Szokoly, G.P. et al. 2004, ApJS, 155, 271
Tozzi, P. et al. 2001, AJ, 562, 42
Tozzi, P., Gilli, R., Mainieri, V. et al. 2006, A&A in press, [astro-ph/0602127]
Trump, J. et al. 2007, ApJS, this volume
Turner, T.J. & Punds, K.A. 1989, MNRAS, 240, 833
Turner, T.J. et al.1997, ApJS, 113, 23
Worsley, M.A. et al.2004, MNRAS, 357, 1281
Zakamska, N.L. et al.2003, AJ, 129, 1212

TABLE 4
X-RAY SPECTRAL FIT PARAMETERS

IAU[a]	XID[b]	RA[c] (J2000)	Dec[c]	counts[d] [0.3-10]	z[e]	MODEL[f]	Γ	N_H	fx[g] [0.5-2]	fx[g] [2-10]	fx[g] [0.5-10]	L_X[h] [0.5-2]	L_X[h] [2-10]	L_X[h] [0.5-10]
XMMC_J100025.30+015851.2	1	10:00:25.30	1:58:51.19	4396	0.373	PL	$2.11^{2.15}_{2.08}$	.....	746.88	795.94	1542.80	43.55	43.58	43.87
XMMC_J095857.50+021314.1	2	9:58:57.50	2:13:14.10	1896	1.024	PL	$1.79^{1.84}_{1.75}$	.....	1178.70	2004.80	3183.60	44.81	45.05	45.25
XMMC_J095902.83+021906.8	3	9:59:02.83	2:19:06.77	2683	0.345	PL	$2.07^{2.12}_{2.03}$	.....	1318.50	1484.60	2803.10	43.72	43.77	44.05
XMMC_J095858.68+021458.1	4	9:58:58.68	2:14:58.12	1188	0.132	PL	$1.78^{1.84}_{1.71}$	.....	851.43	1491.50	2342.90	42.59	42.84	43.03
XMMC_J095918.91+020951.3	5	9:59:18.91	2:09:51.26	1517	1.154	PL	$1.78^{1.84}_{1.72}$	.....	377.01	659.48	1036.50	44.45	44.69	44.89
XMMC_J100043.26+020636.6	6	10:00:43.26	2:06:36.56	1664	0.360	PL	$2.18^{2.26}_{2.11}$	.....	388.08	377.01	765.09	43.25	43.23	43.54
XMMC_J100013.02+023521.8	8	10:00:13.02	2:35:21.82	1121	0.699	PL	$2.45^{2.53}_{2.38}$	.....	627.74	407.25	1035.00	44.13	43.95	44.35
XMMC_J095940.86+021938.6	9	9:59:40.86	2:19:38.56	1094	1.459	PL	$1.99^{2.08}_{1.91}$	.....	196.07	249.26	445.33	44.42	44.52	44.77
XMMC_J100034.95+020234.0	11	10:00:34.95	2:02:34.03	789	1.177	PL	$2.25^{2.37}_{2.13}$	.....	139.90	122.46	262.35	44.04	43.98	44.31
XMMC_J100049.95+020500.0	12	10:00:49.95	2:05:00.03	741	1.235	PL	$2.50^{2.63}_{2.38}$	.....	240.22	144.84	385.06	44.33	44.11	44.53
XMMC_J095924.69+015954.5	17	9:59:24.69	1:59:54.45	1771	1.236	PL	$2.23^{2.30}_{2.16}$	.....	728.21	653.76	1382.00	44.81	44.76	45.09
XMMC_J095958.60+021531.0	19	9:59:58.60	2:15:31.02	487	0.658	PL	$2.05^{2.20}_{1.90}$	.....	247.59	278.06	525.65	43.63	43.70	43.97
XMMC_J100058.80+022556.7	20	10:00:58.80	2:25:56.68	575	0.693	PL	$2.22^{2.34}_{2.10}$	.....	182.66	165.75	348.41	43.62	43.58	43.90
XMMC_J100055.46+023442.0	21	10:00:55.46	2:34:41.99	571	1.403	PL	$2.15^{2.28}_{2.02}$	.....	158.63	159.81	318.44	44.28	44.29	44.58
XMMC_J100046.85+020405.2	22	10:00:46.85	2:04:05.25	586	0.552	PL	$2.70^{2.84}_{2.56}$	.....	113.30	51.61	164.91	43.11	42.77	43.27
XMMC_J095909.63+021917.2	23	9:59:09.63	2:19:17.22	891	0.378	PL	$2.05^{2.16}_{1.95}$	.....	314.47	360.31	674.78	43.17	43.23	43.50
XMMC_J100024.74+023148.3	24	10:00:24.74	2:31:48.34	382	1.318	PL	$2.65^{2.79}_{2.51}$	.....	293.47	143.55	437.02	44.48	44.17	44.66
XMMC_J100024.55+020618.5	25	10:00:24.55	2:06:18.48	440	2.281	PL	$1.75^{1.88}_{1.62}$	.....	156.54	286.15	442.68	44.79	45.06	45.25
XMMC_J095949.51+020139.1	30	9:59:49.51	2:01:39.09	611	1.758	PL	$2.51^{2.67}_{2.35}$	.....	120.90	72.33	193.24	44.41	44.18	44.61
XMMC_J095947.05+022209.4	31	9:59:47.05	2:22:09.38	700	0.909	PL	$2.27^{2.40}_{2.15}$	.....	128.42	108.14	236.56	43.72	43.65	43.99
XMMC_J100114.36+022357.5	33	10:01:14.36	2:23:57.47	410	1.799	PL	$2.34^{2.50}_{2.19}$	.....	119.16	91.12	210.28	44.42	44.31	44.67
XMMC_J095958.62+021805.9	34	9:59:58.62	2:18:05.92	521	1.792	PL	$1.99^{2.14}_{1.85}$	.....	111.88	142.74	254.62	44.39	44.50	44.75
XMMC_J095928.45+022107.6	35	9:59:28.45	2:21:07.64	440	0.346	PL	$2.54^{2.68}_{2.40}$	.....	117.30	67.04	184.34	42.72	42.47	42.91
XMMC_J095940.18+022306.3	37	9:59:40.18	2:23:06.28	698	1.132	PL	$2.16^{2.29}_{2.06}$	.....	89.97	89.38	179.35	43.81	43.80	44.10
XMMC_J100058.94+015359.5	38	10:00:58.94	1:53:59.45	369	1.559	APL	$2.04^{2.19}_{1.85}$	$20.73^{21.46}_{20.42}$	106.94	129.53	236.47	44.32	44.39	44.65
XMMC_J100114.94+020208.9	40	10:01:14.94	2:02:08.93	602	0.989	PL	$2.01^{2.14}_{1.89}$	.....	465.40	574.11	1039.50	44.37	44.47	44.72
XMMC_J100025.43+020734.4	41	10:00:25.43	2:07:34.43	315	0.114	APL+po	$1.95^{2.37}_{1.65}$	$21.51^{21.55}_{21.27}$	76.89	204.98	281.87	41.63	41.76	42.00
XMMC_J100202.80+022435.8	42	10:02:02.80	2:24:35.82	476	0.988	PL	$2.15^{2.32}_{1.99}$	.....	197.35	197.84	395.20	44.00	44.00	44.30
XMMC_J100051.57+021215.8	44	10:00:51.57	2:12:15.80	305	1.829	PL	$2.14^{2.32}_{1.99}$	.....	105.65	107.47	213.13	44.39	44.40	44.69
XMMC_J100014.12+020054.2	51	10:00:14.12	2:00:54.18	336	2.497	PL	$1.98^{2.26}_{1.88}$	.....	50.78	65.43	116.21	44.44	44.55	44.80
XMMC_J100016.35+015104.3	52	10:00:16.35	1:51:04.30	297	1.135	PL	$1.85^{2.00}_{1.70}$	.....	107.96	169.84	277.80	43.82	44.02	44.23
XMMC_J100131.15+022924.8	54[i]	10:01:31.15	2:29:24.82	246	0.350	R-S	.....	.....	90.18	24.44	114.62	42.57	42.00	42.67
XMMC_J100001.16+021413.9	56	10:00:01.16	2:14:13.92	110	1.407	PL	2.00	.....	89.25	101.56	190.81	44.04	44.09	44.37
XMMC_J100047.09+020017.7	59	10:00:47.09	2:00:17.71	226	1.904	PL	$2.12^{2.33}_{2.03}$	.....	59.74	63.30	123.04	44.18	44.21	44.50
XMMC_J095907.84+020819.3	63	9:59:07.84	2:08:19.34	264	0.354	PL	$1.95^{2.19}_{1.73}$	.....	193.50	260.69	454.19	42.85	42.98	43.22
XMMC_J095934.63+020627.9	64	9:59:34.63	2:06:27.94	299	0.686	PL	$1.64^{1.81}_{1.47}$	.....	56.23	121.35	177.58	43.00	43.34	43.50
XMMC_J100041.87+022411.1	65	10:00:41.87	2:24:11.07	122	0.979	PL	2.00	.....	61.79	77.64	139.44	43.49	43.59	43.84
XMMC_J095928.45+021950.5	66	9:59:28.45	2:19:50.47	436	1.488	PL	$2.22^{2.40}_{2.04}$	.....	81.58	74.39	155.96	44.06	44.02	44.34
XMMC_J100137.74+022845.1	67	10:01:37.74	2:28:45.09	224	0.367	PL	$1.93^{2.16}_{1.71}$	.....	69.35	97.21	166.56	42.37	42.51	42.75
XMMC_J095934.92+021028.5	69	9:59:34.92	2:10:28.46	133	2.412	PL	2.00	.....	78.25	98.32	176.57	44.55	44.65	44.91
XMMC_J100036.13+022830.7	70	10:00:36.13	2:28:30.66	181	0.688	APL	$2.78^{3.92}_{2.27}$	$23.23^{23.41}_{23.04}$	25.19	579.88	605.07	44.68	44.29	44.83
XMMC_J100129.81+023239.6	72	10:01:29.81	2:32:39.56	220	0.825	APL	$1.72^{2.04}_{1.40}$	$21.00^{21.47}_{20.42}$	55.72	114.19	169.91	43.33	43.61	43.80
XMMC_J100031.66+014757.4	75	10:00:31.66	1:47:57.40	363	1.681	PL	$1.94^{2.10}_{1.80}$	.....	154.44	211.03	365.48	44.46	44.60	44.84
XMMC_J100028.71+021744.5	78	10:00:28.71	2:17:44.48	203	1.039	PL	$1.72^{2.02}_{1.45}$	.....	50.69	95.86	146.54	43.46	43.74	43.93
XMMC_J100124.93+022032.2	79	10:01:24.93	2:20:32.19	171	1.708	PL	2.00	.....	74.53	93.65	168.18	44.16	44.26	44.52
XMMC_J100105.65+015603.0	81	10:01:05.65	1:56:03.04	285	0.915	APL	$1.44^{1.65}_{1.23}$	$21.44^{21.67}_{20.94}$	50.50	159.64	210.14	43.26	43.70	43.84
XMMC_J100117.73+023309.0	85	10:01:17.73	2:33:09.02	184	1.001	APL	$1.99^{2.42}_{1.58}$	$21.16^{21.63}_{20.42}$	50.33	68.88	119.21	43.50	43.60	43.85
XMMC_J100048.01+021128.0	94	10:00:48.01	2:11:28.00	142	1.515	PL	2.00	.....	80.93	101.69	182.61	44.07	44.17	44.43
XMMC_J100136.47+025304.5	96	10:01:36.47	2:53:04.50	134	2.117	PL	2.00	.....	163.26	201.31	364.57	44.73	44.83	45.08

TABLE 4 — *Continued*

IAU[a]	XID[b]	RA[c] (J2000)	Dec[c]	counts[d] [0.3-10]	z[e]	MODEL[f]	Γ	N_H	fx[g] [0.5-2]	fx[g] [2-10]	fx[g] [0.5-10]	L_X[h] [0.5-2]	L_X[h] [2-10]	L_X[h] [0.5-10]
XMMC_J100031.41+022819.2	101	10:00:31.41	2:28:19.18	131	0.926	PL	2.00	.....	47.26	59.38	106.63	43.31	43.41	43.66
XMMC_J100028.20+015547.0	103	10:00:28.20	1:55:46.98	144	1.519	PL	2.00	.....	53.96	67.80	121.76	43.90	44.00	44.25
XMMC_J100038.13+022455.8	106	10:00:38.13	2:24:55.79	141	0.710	APL+po	2.00	$22.33^{22.66}_{21.98}$	14.54	43.92	58.47	42.85	42.95	43.20
XMMC_J095935.73+020537.2	113	9:59:35.73	2:05:37.24	101	1.910	PL	2.00	.....	55.61	69.87	125.48	44.16	44.26	44.51
XMMC_J100210.73+023028.0	115	10:02:10.73	2:30:27.97	591	1.161	APL	$2.10^{2.23}_{1.95}$	$21.10^{21.42}_{20.42}$	176.22	204.96	381.18	44.18	44.22	44.50
XMMC_J100049.61+021709.2	116	10:00:49.61	2:17:09.17	218	0.874	APL	$2.11^{2.38}_{1.61}$	$21.11^{21.58}_{20.42}$	74.38	87.32	161.71	43.53	43.56	43.84
XMMC_J100013.45+021400.5	117	10:00:13.45	2:14:00.47	111	0.936	APL+po	2.00	$22.76^{23.14}_{22.37}$	28.01	35.20	63.21	43.09	43.19	43.45
XMMC_J100122.23+021334.0	119	10:01:22.23	2:13:33.99	328	0.891	APL	$1.69^{2.04}_{1.40}$	$21.01^{21.48}_{20.42}$	213.98	452.80	666.78	43.97	44.27	44.44
XMMC_J095945.47+021029.9	122	9:59:45.47	2:10:29.88	130	2.418	APL	2.00	$23.69^{23.91}_{23.44}$	14.90	147.41	162.32	44.83	44.93	45.18
XMMC_J100131.93+023335.5	123	10:01:31.93	2:33:35.46	142	2.065	PL	2.00	.....	23.93	30.07	54.00	43.87	43.97	44.23
XMMC_J100001.27+022320.7	127	10:00:01.27	2:23:20.69	217	1.846	PL	$2.55^{2.91}_{2.22}$	.....	34.62	19.63	54.25	43.91	43.67	44.11
XMMC_J100047.85+020756.1	128	10:00:47.85	2:07:56.15	120	2.161	PL	2.00	.....	32.52	40.86	73.38	44.06	44.15	44.41
XMMC_J100100.90+015946.7	129	10:01:00.90	1:59:46.69	184	1.170	PL	$1.98^{2.21}_{1.76}$	.....	196.94	256.78	453.72	44.13	44.25	44.49
XMMC_J100105.36+021348.0	133	10:01:05.36	2:13:47.96	144	2.627	PL	2.00	.....	56.73	71.28	128.00	44.50	44.60	44.86
XMMC_J100011.78+021919.9	134	10:00:11.78	2:19:19.86	141	0.625	PL	2.00	.....	35.13	44.14	79.28	42.76	42.86	43.12
XMMC_J095949.98+020010.6	137	9:59:49.98	2:00:10.57	195	1.808	PL	$1.87^{2.31}_{1.48}$	.....	44.24	92.96	137.20	44.06	44.25	44.47
XMMC_J100033.55+015236.3	141	10:00:33.55	1:52:36.34	102	0.831	APL	2.00	$21.64^{21.96}_{21.19}$	51.21	85.40	136.61	43.36	43.45	43.71
XMMC_J100013.46+022656.7	143	10:00:13.46	2:26:56.66	140	0.732	APL	2.00	$22.68^{23.06}_{22.38}$	29.41	194.21	223.62	43.62	43.72	43.97
XMMC_J095938.49+020447.5	146	9:59:38.49	2:04:47.51	167	2.804	APL	2.00	$21.95^{22.26}_{21.23}$	53.36	73.96	127.32	44.59	44.69	44.94
XMMC_J100053.93+021614.2	147	10:00:53.93	2:16:14.22	112	2.944	PL	2.00	.....	26.82	33.70	60.52	44.30	44.40	44.65
XMMC_J100052.57+021643.8	148	10:00:52.57	2:16:43.80	111	0.843	PL	2.00	.....	41.34	51.94	93.27	43.15	43.25	43.50
XMMC_J100124.00+021446.4	152	10:01:24.00	2:14:46.45	172	0.894	PL	2.00	.....	88.13	110.74	198.87	43.54	43.64	43.90
XMMC_J100108.44+022342.6	153	10:01:08.44	2:23:42.58	142	1.928	APL	2.00	$21.91^{22.20}_{21.40}$	33.00	49.24	82.24	44.02	44.12	44.37
XMMC_J100108.59+020053.2	161	10:01:08.59	2:00:53.24	254	2.681	PL	$1.69^{1.93}_{1.46}$	.....	75.27	149.97	225.25	44.65	44.95	45.12
XMMC_J100118.55+015543.6	164	10:01:18.55	1:55:43.59	291	0.528	PL	$2.54^{2.73}_{2.36}$	.....	176.15	100.11	276.25	43.32	43.07	43.51
XMMC_J100043.30+021352.7	165	10:00:43.30	2:13:52.65	120	2.146	PL	2.00	.....	25.58	32.14	57.73	43.94	44.04	44.30
XMMC_J095917.44+021514.9	170	9:59:17.44	2:15:14.91	142	0.935	PL	2.00	.....	37.05	46.55	83.59	43.21	43.31	43.57
XMMC_J100128.19+021819.9	171	10:01:28.19	2:18:19.86	133	1.187	PL	2.00	.....	34.80	43.72	78.52	43.44	43.54	43.80
XMMC_J095921.15+020030.8	196	9:59:21.15	2:00:30.83	154	1.486	PL	2.00	.....	56.39	70.85	127.24	43.89	43.99	44.25
XMMC_J100047.93+014935.9	198	10:00:47.93	1:49:35.93	134	0.893	PL	2.00	.....	46.55	58.49	105.04	43.26	43.36	43.62
XMMC_J095858.95+020138.7	199	9:58:58.95	2:01:38.72	268	2.454	PL	$2.11^{2.36}_{1.92}$	.....	161.11	171.30	332.41	44.88	44.91	45.20
XMMC_J100105.90+015918.6	206	10:01:05.90	1:59:18.58	131	0.721	APL	2.00	$21.69^{22.19}_{20.99}$	29.60	53.14	82.74	43.00	43.10	43.35
XMMC_J100058.47+015206.4	216	10:00:58.47	1:52:06.40	216	2.029	PL	$2.22^{2.69}_{1.84}$	.....	42.84	39.07	81.91	44.11	44.07	44.39
XMMC_J095956.08+014728.0	222	9:59:56.08	1:47:27.97	237	0.337	PL	$2.28^{2.57}_{2.01}$	.....	73.53	61.26	134.79	42.57	42.49	42.83
XMMC_J100139.88+023132.8	236	10:01:39.88	2:31:32.77	110	1.444	PL	2.00	.....	12.81	16.09	28.90	43.22	43.32	43.57
XMMC_J100046.86+014737.1	256	10:00:46.86	1:47:37.14	113	1.867	APL	2.00	$20.71^{21.83}_{20.42}$	55.75	70.92	126.67	44.22	44.32	44.57
XMMC_J100042.36+014535.7	265	10:00:42.36	1:45:35.66	101	1.161	PL	2.00	.....	38.62	48.52	87.14	43.47	43.56	43.82
XMMC_J095910.00+022018.4	268	9:59:10.00	2:20:18.42	143	0.432	APL	2.00	$21.32^{21.60}_{20.89}$	34.78	56.34	91.12	42.49	42.59	42.84
XMMC_J100005.52+023057.4	274	10:00:05.52	2:30:57.40	112	0.677	APL+po	2.00	$22.67^{23.00}_{22.18}$	18.30	104.83	123.13	43.26	43.36	43.62
XMMC_J095929.40+022035.6	282	9:59:29.40	2:20:35.60	150	1.733	PL	2.00	.....	18.24	22.92	41.16	43.57	43.67	43.92
XMMC_J095902.45+022510.6	288	9:59:02.45	2:25:10.61	202	1.105	PL	$2.17^{2.46}_{1.91}$	.....	35.06	34.23	69.29	43.30	43.29	43.60
XMMC_J095927.04+015340.8	293	9:59:27.04	1:53:40.84	222	0.444	APL	$1.51^{2.10}_{1.21}$	$21.91^{22.13}_{21.70}$	136.15	666.98	803.13	43.28	43.69	43.83
XMMC_J100016.65+021352.1	298	10:00:16.65	2:13:52.11	100	1.867	PL	2.00	.....	23.63	29.70	53.33	43.76	43.86	44.11
XMMC_J100049.94+015230.8	359	10:00:49.94	1:52:30.79	222	1.156	PL	$1.54^{1.85}_{1.28}$	.....	35.99	89.17	125.16	43.35	43.74	43.89
XMMC_J100118.89+020729.0	391	10:01:18.89	2:07:28.98	110	1.774	PL	2.00	.....	50.15	62.98	113.13	44.03	44.13	44.39
XMMC_J100006.35+023342.0	398	10:00:06.35	2:33:42.01	131	0.745	APL	2.00	$21.64^{21.98}_{21.19}$	40.43	69.95	110.38	43.15	43.25	43.51
XMMC_J095944.64+022626.2	416	9:59:44.64	2:26:26.22	102	0.992	APL	2.00	$22.19^{22.57}_{21.72}$	18.76	45.28	64.04	43.28	43.38	43.63
XMMC_J100223.07+014715.1	2013	10:02:23.07	1:47:15.07	686	1.243	PL	$1.82^{1.92}_{1.73}$	.....	428.34	700.54	1128.90	44.58	44.80	45.00
XMMC_J095819.89+022903.8	2016	9:58:19.89	2:29:03.78	768	0.345	PL	$2.19^{2.31}_{2.07}$	.....	385.27	373.31	758.58	43.21	43.19	43.50
XMMC_J100234.40+015011.5	2020	10:02:34.40	1:50:11.51	651	1.506	PL	$2.25^{2.37}_{2.14}$	.....	226.06	196.73	422.80	44.51	44.45	44.78
XMMC_J100129.41+013633.7	2021	10:01:29.41	1:36:33.75	271	0.104	APL	$1.23^{1.39}_{1.01}$	$22.38^{22.51}_{22.24}$	163.24	4230.20	4393.50	42.39	43.12	43.19

TABLE 4 — *Continued*

IAU[a]	XID[b]	RA[c] (J2000)	Dec[c]	counts[d] [0.3-10]	z[e]	MODEL[f]	Γ	N_H	fx[g] [0.5-2]	fx[g] [2-10]	fx[g] [0.5-10]	L_X[h] [0.5-2]	L_X[h] [2-10]	L_X[h] [0.5-10]
XMMC_J100211.31+013707.2	2028	10:02:11.31	1:37:07.15	293	0.784	APL+Fe	$2.55^{2.79}_{2.29}$	$21.83^{21.95}_{21.69}$	113.12	204.74	317.86	43.75	43.50	43.94
XMMC_J100257.55+015405.6	2036	10:02:57.55	1:54:05.58	233	0.971	PL	$1.89^{2.07}_{1.71}$	.....	284.95	423.49	708.44	44.14	44.31	44.54
XMMC_J100033.51+013812.6	2040	10:00:33.51	1:38:12.61	317	0.520	PL	$2.28^{2.47}_{2.10}$	.....	263.04	212.05	475.09	43.40	43.32	43.67
XMMC_J100237.09+014648.3	2043	10:02:37.09	1:46:48.33	347	0.668	APL+Fe	$1.56^{1.92}_{1.31}$	$21.77^{21.96}_{21.52}$	172.69	608.59	781.28	43.55	43.93	44.08
XMMC_J100303.04+015209.2	2046	10:03:03.04	1:52:09.19	341	1.800	PL	$2.23^{2.43}_{2.04}$	.....	132.62	119.47	252.09	44.47	44.43	44.75
XMMC_J100151.19+020032.8	2058	10:01:51.19	2:00:32.81	779	0.964	PL	$2.02^{2.13}_{1.91}$	.....	285.44	348.97	634.41	44.13	44.22	44.48
XMMC_J100229.27+014528.2	2071	10:02:29.27	1:45:28.21	328	0.876	PL	$1.58^{1.73}_{1.44}$	.....	177.16	414.17	591.34	43.72	44.09	44.24
XMMC_J100141.42+021031.8	2078	10:01:41.42	2:10:31.78	195	0.982	APL	$1.93^{2.20}_{1.59}$	$20.96^{21.50}_{20.42}$	135.04	197.89	332.93	43.85	44.00	44.23
XMMC_J100238.78+013938.2	2080	10:02:38.78	1:39:38.25	238	1.315	PL	$1.87^{2.02}_{1.73}$	.....	127.19	193.62	320.82	44.07	44.26	44.48
XMMC_J100238.27+013747.8	2093	10:02:38.27	1:37:47.75	222	2.506	PL	$1.97^{2.16}_{1.79}$	.....	131.93	172.73	304.66	44.82	44.94	45.18
XMMC_J100214.21+020620.0	2096	10:02:14.21	2:06:20.02	482	1.265	PL	$1.64^{1.75}_{1.54}$	.....	131.85	282.01	413.85	44.03	44.36	44.53
XMMC_J100219.58+015536.9	2105	10:02:19.58	1:55:36.94	323	1.509	PL	$2.19^{2.43}_{1.97}$	.....	74.17	70.26	144.43	44.03	44.01	44.32
XMMC_J100305.20+015157.0	2118	10:03:05.20	1:51:57.04	195	0.969	APL	$2.14^{2.61}_{1.75}$	$20.99^{21.58}_{20.42}$	165.82	180.69	346.51	43.93	43.94	44.24
XMMC_J095848.84+023442.3	2138	9:58:48.84	2:34:42.34	729	1.551	PL	$2.01^{2.11}_{1.90}$	.....	121.90	151.84	273.74	44.28	44.37	44.63
XMMC_J100230.13+014810.0	2152	10:02:30.13	1:48:10.01	281	0.626	PL	$2.21^{2.57}_{1.90}$	.....	94.64	86.97	181.61	43.19	43.16	43.48
XMMC_J100232.55+014009.5	2169	10:02:32.55	1:40:09.53	144	1.776	PL	2.00	.....	72.41	90.98	163.39	44.19	44.29	44.55
XMMC_J100141.11+021259.9	2191	10:01:41.11	2:12:59.88	225	0.621	PL	$2.27^{2.53}_{2.03}$	.....	87.36	74.02	161.38	43.01	42.94	43.28
XMMC_J100236.79+015948.5	2202	10:02:36.79	1:59:48.50	142	1.516	PL	2.00	.....	65.21	79.78	144.99	43.98	44.07	44.33
XMMC_J100038.40+013708.4	2211	10:00:38.40	1:37:08.37	153	1.251	PL	2.00	.....	65.00	81.68	146.68	43.77	43.87	44.13
XMMC_J100156.40+014811.0	2213	10:01:56.40	1:48:11.00	263	0.957	APL	$2.02^{2.53}_{1.64}$	$20.87^{21.55}_{20.42}$	71.18	91.34	162.52	43.54	43.63	43.89
XMMC_J100226.77+014052.1	2218	10:02:26.77	1:40:52.05	123	0.247	PL	2.00	.....	55.24	69.41	124.65	42.01	42.11	42.36
XMMC_J100041.57+013658.7	2220	10:00:41.57	1:36:58.69	162	0.995	PL	2.00	.....	73.60	92.48	166.08	43.58	43.68	43.93
XMMC_J100156.31+020942.9	2232	10:01:56.31	2:09:42.91	131	1.641	PL	2.00	.....	43.15	54.21	97.36	43.88	43.98	44.24
XMMC_J100253.16+013457.8	2235	10:02:53.16	1:34:57.85	100	2.248	PL	2.00	.....	65.71	81.11	146.82	44.40	44.49	44.75
XMMC_J095904.34+022552.8	2237	9:59:04.34	2:25:52.75	192	0.941	APL	$1.78^{2.41}_{1.40}$	$22.74^{22.96}_{22.55}$	38.88	285.86	324.74	43.91	44.15	44.34
XMMC_J100223.02+020639.5	2246	10:02:23.02	2:06:39.48	303	0.899	PL	$1.95^{2.15}_{1.76}$	.....	69.93	94.68	164.61	43.41	43.54	43.78
XMMC_J100243.88+020501.6	2261	10:02:43.88	2:05:01.59	206	1.234	PL	$1.97^{2.27}_{1.70}$	.....	72.98	95.93	168.91	43.81	43.93	44.17
XMMC_J100208.53+014553.7	2276	10:02:08.53	1:45:53.65	111	2.215	PL	2.00	.....	31.49	39.56	71.05	44.07	44.17	44.42
XMMC_J100158.05+014621.7	2289	10:01:58.05	1:46:21.74	122	0.831	APL	2.00	$22.77^{22.97}_{22.54}$	32.93	230.29	263.22	43.83	43.93	44.19
XMMC_J100130.33+014305.0	2299	10:01:30.33	1:43:04.97	110	1.571	PL	2.00	.....	76.83	96.53	173.35	44.09	44.19	44.44
XMMC_J100143.54+015606.2	2361	10:01:43.54	1:56:06.18	195	2.181	PL	$1.94^{2.24}_{1.68}$	.....	93.06	127.11	220.17	44.52	44.66	44.90
XMMC_J100240.34+020146.4	2370	10:02:40.34	2:01:46.37	132	0.638	APL	2.00	$22.16^{22.69}_{21.76}$	34.05	103.02	137.07	43.17	43.27	43.52
XMMC_J100141.54+020051.4	2557	10:01:41.54	2:00:51.44	120	2.277	PL	2.00	.....	158.62	199.31	357.93	44.80	44.90	45.15
XMMC_J100142.26+020358.5	2608	10:01:42.26	2:03:58.49	131	0.125	PEXRAV+Fe	2.00	>24.18	28.99	511.11	63.12	41.07	42.32	43.87
XMMC_J100136.21+015442.5	2703	10:01:36.21	1:54:42.45	151	2.281	PL	2.00	.....	209.26	262.93	472.19	44.92	45.02	45.27

[a] IAU name. [b] Internal reference number. [c] X-ray coordinates. [d] Net *pn* counts in the [0.3-10] keV energy band. [e] Spectroscopic redshift of the most likely optical counterpart (for details see **?**). [f] Best fit model as discussed in §4. [g] X-ray fluxes from the spectral fit in units of 10^{-16} erg cm^{-2} s^{-1} in the [0.5-2], [2-10] and [0.5-10] keV rest-frame energy bands respectively [h] Logarithm of the X-ray luminosities corrected for absorption in the [0.5-2], [2-10] and [0.5-10] keV rest-frame energy bands respectively. [i] A powerlaw model is not a good representation of this source(see §4.1).

TABLE 5
Comparison between optical and X-ray classifications

	Broad Line AGN	Narrow Line AGN	Galaxy
X-ray unabsorbed AGN	78	19	5
X-ray absorbed AGN	8	13	11
X-ray galaxy	0	0	0